PNAS RESEARCH ARTICLE | PHYSICS OPEN ACCESS

Unraveling the origin of Kondo-like behavior in the 3*d*-electron heavy-fermion compound YFe_2Ge_2

Bing Xu[a,b,c,1,2], Rui Liu[d,1], Hongliang Wo[e], Zhiyu Liao[a,b], Shaohui Yi[a,b], Chunhong Li[a], Jun Zhao[e], Xianggang Qiu[a,b], Zhiping Yin[d,f,2], and Christian Bernhard[c,2]

Affiliations are included on p. 8.

Edited by J.C. Davis, University of Oxford, Oxford, United Kingdom; received January 22, 2024; accepted August 21, 2024

The heavy fermion (HF) state of *d*-electron systems is of great current interest since it exhibits various exotic phases and phenomena that are reminiscent of the Kondo effect in *f*-electron HF systems. Here, we present a combined infrared spectroscopy and first-principles band structure calculation study of the 3*d*-electron HF compound YFe_2Ge_2. The infrared response exhibits several charge-dynamical hallmarks of HF and a corresponding scaling behavior that resemble those of the *f*-electron HF systems. In particular, the low-temperature spectra reveal a dramatic narrowing of the Drude response along with the appearance of a hybridization gap ($\Delta \sim 50$ meV) and a strongly enhanced quasiparticle effective mass. Moreover, the temperature dependence of the infrared response indicates a crossover around $T^* \sim 100$ K from a coherent state at low temperature to a quasi-incoherent one at high temperature. Despite of these striking similarities, our band structure calculations suggest that the mechanism underlying the HF behavior in YFe_2Ge_2 is distinct from the Kondo scenario of the *f*-electron HF compounds and even from that of the *d*-electron iron-arsenide superconductor KFe_2As_2. For the latter, the HF state is driven by orbital-selective correlations due to a strong Hund's coupling. Instead, for YFe_2Ge_2 the HF behavior originates from the band flatness near the Fermi level induced by the combined effects of kinetic frustration from a destructive interference between the direct Fe-Fe and indirect Fe-Ge-Fe hoppings, band hybridization involving Fe 3*d* and Y 4*d* electrons, and electron correlations. This highlights that rather different mechanisms can be at the heart of the HF state in *d*-electron systems.

flat band | heavy fermion | optical conductivity

Significance

We present a combined experimental and theoretical study of the optical conductivity of 3*d*-electron compound YFe_2Ge_2. Our work reveals the presence of a flat band at the Fermi level and related optical features that are typical for heavy fermion (HF) systems. However, unlike the Kondo scenario and its analog driven by strong Hund's coupling, we obtain evidence for an alternative mechanism which accounts for the HF-like response of YFe_2Ge_2 in terms of the combined effects of kinetic frustration, band hybridization, and electron correlations. Our results help to unravel the origin of the HF properties of YFe_2Ge_2 and also provide a broad perspective on the exotic phenomena of other *d*-electron materials with HF-like properties, like some of the iron arsenide superconductors.

The electronic band structure of solids plays a crucial role in determining their physical properties. Flat bands, characterized by a lack of dispersion over sizeable momentum ranges, are particularly intriguing. They typically give rise to an extremely singular density of states (DOS) and superheavy electrons that tend to get localized as the electron–electron Coulomb interaction dominates over the quenched kinetic energy. This provides a fundamental platform for realizing a variety of quantum phenomena (1–9), including magnetism, Mott insulators, density waves, non-Fermi liquid behavior, fractional quantum Hall effect, and unconventional superconductivity. For instance, in moiré materials, like twisted bilayer graphene, the flat bands can be shaped via the twist angle to obtain correlated insulator states and strong-coupling superconductivity (8, 9) for which the phase diagram resembles that of the high-T_c cuprates. Likewise, in a geometrically frustrated kagome lattice, the coexistence of Dirac crossings and flat bands offers an intriguing opportunity to explore novel physics involving both correlation and topology (10). Prominent examples are the recently studied kagome compounds $Co_3Sn_2S_2$ (11, 12), AV_3Sb_5 (A = K, Rb, Cs) (13–15), $TbMn_6Sn_6$ (16), CoSn (17, 18) and FeGe (19). Another prominent example is heavy fermion (HF) materials (20), where a flat band in the vicinity of the Fermi level is achieved via the Kondo hybridization between itinerant conduction electrons and localized *f* electrons.

Beyond the *f*-electron HF materials, there is a growing interest in exploring flat bands and HF states in *d*-electron systems, including compounds like $CaCu_3Ir_4O_{12}$ (21), $CaCu_3Ru_4O_{12}$ (22, 23), $Ca_{2-x}Sr_xRuO_4$ (24), LiV_2O_4 (25), Fe_3GeTe_2 (26), and iron-based superconductors (FeSCs) (27–31). This interest stems from the multiorbital nature of *d*-electrons and their orbital-selective renormalization. In these systems, the electronic correlations, especially Hund's coupling, have different influences on the bands, leading to an enhanced orbital differentiation (29–31). Consequently, the *d*-electron HF-type state can be achieved by doping a Hund's metal with pronounced orbital-selective correlations

Author contributions: B.X. and C.B. designed research; B.X., R.L., H.W., Z.L., S.Y., C.L., J.Z., X.Q., and Z.Y. performed research; B.X., Z.Y., and C.B. analyzed data; and B.X. and C.B. wrote the paper.

The authors declare no competing interest.

This article is a PNAS Direct Submission.

[1]B.X. and R.L contributed equally to this work.

[2]To whom correspondence may be addressed. Email: bingxu@iphy.ac.cn, yinzhiping@bnu.edu.cn, or christian.bernhard@unifr.ch.

This article contains supporting information online at https://www.pnas.org/lookup/suppl/doi:10.1073/pnas.2401430121/-/DCSupplemental.

Published September 19, 2024.

toward half-filling, where carriers on certain orbitals become localized while others remain itinerant, thus resembling the coexistence of light and heavy electrons originating from *s* and *f* orbitals, respectively, in *f*-electron HF systems. Of particular interest are the heavily hole-doped FeSCs AFe_2As_2(A = K, Rb, Cs) of the so-called 122 family. For instance, KFe_2As_2 exhibits a remarkable mass enhancement with a large Sommerfeld coefficient, $\gamma \sim 100$ mJ mol^{-1}K^{-2} (32), comparable to that of *f*-electron HF materials. Quantum oscillation and angle-resolved photoemission spectroscopy (ARPES) experiments also support a strong mass enhancement (33–35). Additionally, a coherence-incoherence crossover, similar to that of *f*-electron HFs, has been observed in KFe_2As_2 (27, 36, 37). The coexistence of itinerant and local characters of the Fe 3*d* electrons, along with the possible interplay of orbital-selective Hund and Kondo physics, make FeSCs a unique paradigm for exploring rich emergent quantum many-body phenomena in *d*-electron HF systems.

YFe_2Ge_2 is the parent compound of a new class of FeSCs, the so-called iron germanides, that is formally isoelectronic to KFe_2As_2 but has a so-called collapsed crystal structure, similar to that of KFe_2As_2 under high pressure (38, 39). YFe_2Ge_2 is thus an interesting reference compound to KFe_2As_2 which may allow one to study the essential features of the *d*-electron HF phenomenon. In YFe_2Ge_2, the resistivity indicates a breakdown of Fermi liquid behavior at low temperatures (39, 40), and unconventional superconductivity (39, 41–43), possibly on the verge of spin-triplet pairing (44), is confirmed at $T_c \sim 1.8$ K. YFe_2Ge_2 is paramagnetic at room temperature with no magnetic phase transition down to the lowest measured temperature. However, large fluctuating magnetic moments have been observed with X-ray photoemission spectroscopy (45) and spin susceptibility measurements (46). Inelastic neutron scattering experiments further revealed the coexistence of anisotropic stripe-type antiferromagnetic (AFM) and isotropic ferromagnetic (FM) spin fluctuations (47). Recent NMR experiments have suggested that YFe_2Ge_2 is likely close to an itinerant magnetic quantum critical point (44). With respect to the HF properties, an unusually high Sommerfeld coefficient $\gamma \sim 100$ mJ mol^{-1}K^{-2} has been measured with specific heat in YFe_2Ge_2 (39, 43). A strong mass enhancement has been also supported by recent quantum oscillation and ARPES experiments (48, 49). A coherence-incoherence crossover has been revealed and attributed to Hund's coupling–induced electronic correlations (44). In addition, a flat band feature near the Fermi level has been observed in the ARPES measurements (49, 50). Regarding the origin of these HF phenomena, there exists no consensus among the various experimental reports. In some cases, they have been attributed to possible Kondo physics (49), while in others they have been interpreted in terms of the orbital-differentiation physics in the Hund's limit (44, 51). This urgently calls for further combined experimental and theoretical studies to clarify the origin of the unusual HF-like properties of YFe_2Ge_2.

In this work, we address this problem with combined infrared spectroscopy and first-principles band structure calculation studies of YFe_2Ge_2. In the infrared response, we identify all the typical features of a *d*-electron HF system, including a very narrow Drude peak due to charge carriers with a strongly enhanced effective mass, a hybridization gap, an electronic crossover from a coherent low temperature to a quasi-incoherent high temperature state, and a characteristic scaling behavior. Nevertheless, our theoretical calculations reveal a distinct mechanism for the emergence of a flat band at the Fermi level and a subsequent *d*-electron HF state in YFe_2Ge_2. Here, the source of band flatness is primarily from a kinetic frustration due to a destructive interference effect between the direct Fe-Fe and indirect Fe-Ge-Fe hopping channels which for the collapsed structure of YFe_2Ge_2 have a similar magnitude but opposite signs. An important role is also played by the band hybridization involving Fe 3*d* and Y 4*d* electrons, whereas the Hund's coupling and the related orbital differentiation of the electron correlations appear to be secondary effects.

Fig. 1*A* shows the temperature dependence of the in-plane reflectivity of YFe_2Ge_2 in the infrared region below 10,000 cm^{-1}.

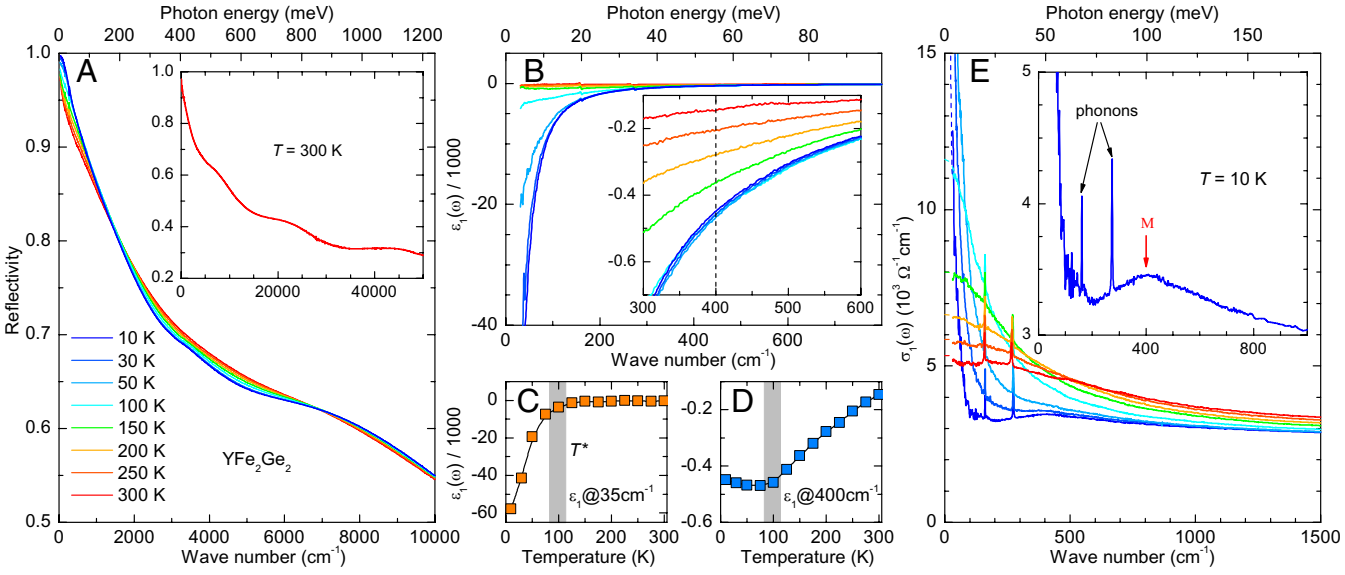

Fig. 1. (*A*) Temperature-dependent reflectivity spectra of YFe_2Ge_2 in the infrared range up to 10,000 cm^{-1}. *Inset*: Reflectivity spectrum at 300 K up to 50,000 cm^{-1}. (*B*) Temperature dependence of the real part of the dielectric function, $\varepsilon_1(\omega)$. *Inset*: Enlarged view of $\varepsilon_1(\omega)$ from 300 to 600 cm^{-1}. (*C*) Temperature dependence of $\varepsilon_1(\omega)$ at 35 cm^{-1} showing a pronounced slope change due to a coherence-incoherence crossover around $T^* \sim 100$ K (gray bar). (*D*) Corresponding temperature dependence of $\varepsilon_1(\omega)$ at 400 cm^{-1}. (*E*) Temperature-dependent spectra of the optical conductivity, $\sigma_1(\omega)$, up to 1,500 cm^{-1} revealing a narrow Drude peak and a low-energy band around 400 cm^{-1} that emerges below $T^* \sim 100$ K. Dashed lines show extrapolations to zero frequency. *Inset*: Magnified view of the 10 K spectrum highlighting the very narrow Drude peak, the band around 400 cm^{-1} (M) and two infrared-active phonons.

The *Inset* displays the room-temperature spectrum over the full measured range up to 50,000 cm^{-1}. The overall shape of the reflectivity curves, with a zero-frequency value close to unity, signals a metallic response with a moderate screened plasma frequency of about 3,000 cm^{-1}. In the following, we discuss the electronic response and its changes with temperature in terms of the dielectric function and the related optical conductivity that have been derived from the reflectivity spectra.

Fig. 1*B* displays the temperature-dependent spectra of the real part of the dielectric function, $\varepsilon_1(\omega)$, in the far-infrared region. The overall negative values of $\varepsilon_1(\omega)$ are characteristic of the inductive response of a metal. Notably, at frequencies below about 200 cm^{-1}, the spectra undergo some drastic changes at low temperatures. Whereas above 100 K, $\varepsilon_1(\omega)$ levels off at low frequencies, implying a rather large scattering rate, below 100 K it exhibits a sharp decrease with $\varepsilon_1(\omega) \sim -1/\omega^2$, which signifies a major reduction of the scattering rate. This characteristic behavior indicates a temperature-induced crossover of the charge dynamics from a high-temperature quasi incoherent to a low-temperature coherent state. As shown in Fig. 1*C*, the crossover temperature $T^* \sim 100$ K can be readily determined from the sudden slope change in the temperature dependence of the low-frequency value $\varepsilon_1(35\ cm^{-1})$, as marked by a gray bar. Fig. 1*D* displays the corresponding temperature dependence of $\varepsilon_1(400\ cm^{-1})$ which shows that the sudden decrease of $\varepsilon_1(\omega)$ below $T^* \sim 100$ K occurs only at very low frequencies, meaning that the screened plasma frequency of the weakly scattered carriers is less than 400 cm^{-1}. The value of $\varepsilon_1(400\ cm^{-1})$ exhibits instead a weak upturn below T^* which arises from a new low-energy electronic band that emerges in the low-temperature coherent state. This band with a maximum around 400 cm^{-1} is also seen in the corresponding spectra of the real part of the optical conductivity, $\sigma_1(\omega)$, in Fig. 1*E*, where it is marked in the *Inset* by a red arrow (M). The latter also details two sharp infrared-active phonon modes around 160 cm^{-1} and 270 cm^{-1}.

The $\sigma_1(\omega)$ spectra in Fig. 1*E* confirm the above-described strong narrowing of the Drude response below 100 K. At high temperature, they reveal a rather broad Drude peak with a strong tail toward high frequencies, due to intraband excitations of carriers with a large scattering rate that are quasi incoherent. Toward lower temperature, the Drude peak shows a pronounced narrowing effect that signals a strong reduction of the scattering rate, i.e., its low-frequency head gets strongly enhanced while the high-frequency tail decreases correspondingly. In particular, below $T^* \sim 100$ K the Drude peak becomes very sharp and resembles that typically observed in HF systems (52). The infrared spectra thus signal a rather sudden change in the charge dynamics of YFe_2Ge_2 from a quasi incoherent high-temperature state with a large scattering rate, to a coherent state with a very small scattering rate below T^*.

Fig. 2*A* displays the temperature-dependent $\sigma_1(\omega)$ spectra for a wider frequency range up to 10,000 cm^{-1}, which includes two pronounced interband transitions. The latter give rise to bands with maxima around 3,500 cm^{-1} and 6,500 cm^{-1}, which in the following are denoted as α and β bands. This double-peak structure also shows a substantial variation with temperature. With increasing temperature, the α and β bands both become broader. However, whereas the α band moves to slightly higher energy, the β band is shifted toward lower energy. Likewise, the spectral weight of the α peak increases, while that of the β peak decreases. These trends lead to a gradual blurring of the double-peak structure at elevated temperatures.

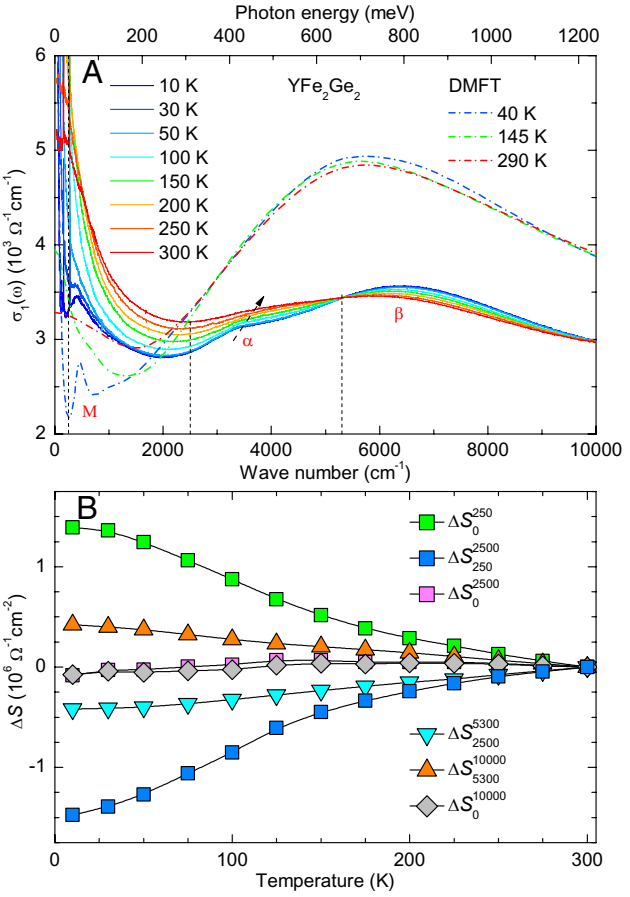

Fig. 2. (*A*) Temperature-dependent spectra of the optical conductivity, $\sigma_1(\omega)$, in the infrared range up to 10,000 cm^{-1}. Dashed lines show the conductivity obtained from DFT + DMFT calculations. (*B*) Temperature dependence of the spectral weight changes, $\Delta S(T) = S(T) - S(300\ K)$, for different frequency ranges with the cutoff frequencies marked by the vertical dashed lines in panel (*A*).

The above-described temperature-dependent changes of the electronic response have been further analyzed in terms of the partial spectral weight, $S_{\omega_a}^{\omega_b}(T) = \int_{\omega_a}^{\omega_b} \sigma_1(\omega, T)d\omega$, within certain frequency ranges as defined by the lower and upper cutoff frequencies ω_a and ω_b, respectively. For suitable choices of ω_a and ω_b, as shown by the dashed lines in Fig. 2*A*, this allows us to specify the spectral weight changes of the different electronic excitations, i.e., of the Drude peak in the ranges from 0 to 250 cm^{-1} and from 250 to 2,500 cm^{-1}, of the α band from 2,500 to 5,300 cm^{-1}, and of the β band between 5,300 and 10,000 cm^{-1}. Fig. 2*B* details the spectral weight changes with respect to the room temperature value, $\Delta S(T) = S(T) - S(300\ K)$, for the various cutoff frequencies. In the ranges of 0 to 250 cm^{-1} and 250 to 2,500 cm^{-1}, that are governed by the coherent and incoherent excitations of the free carriers, respectively, the incoherence-coherence crossover leads to an increase of ΔS_0^{250} and a corresponding decrease of $\Delta S_{250}^{2,500}$. Notably, the reduction in $\Delta S_{250}^{2,500}$ almost matches the enhancement in ΔS_0^{250}, as confirmed by the almost temperature-independent value of $\Delta S_0^{2,500}$. This conservation of the partial spectral weight below 2,500 cm^{-1} confirms that this low-energy range is governed by a Drude-type response with a rather broad and strongly temperature-dependent tail. Correspondingly, for

the frequency ranges of 2,500 to 5,300 cm^{-1} and 5,300 to 10,000 cm^{-1}, that are dominated by the α and β excitations, respectively, it is evident that the decrease of $\Delta S^{5,300}_{2,500}$ is almost compensated by the rise of $\Delta S^{10,000}_{5,300}$, such that $\Delta S^{10,000}_{2,500}$ and $\Delta S^{10,000}_{0}$ remain almost constant.

A quantitative analysis of the temperature evolution of the various intra- and interband excitations has been obtained with a Drude–Lorentz model fit of the $\sigma_1(\omega)$ spectra. A comprehensive description of the Drude–Lorentz model is provided in *SI Appendix*, section B. Fig. 3 *A* and *B* detail the decomposition of the $\sigma_1(\omega)$ spectra at $T = 100$ K and 10 K, respectively, with the contribution of the various electronic bands shown in different colors. It confirms that the low-energy part of the spectra is well accounted for by two Drude components: a narrow one (D1 in green) with a small scattering rate and a broad one (D2 in blue) with a very large scattering rate. At $T = 100$ K these scattering rates amount to $1/\tau \sim 174$ cm^{-1} and 3,400 cm^{-1}, respectively. Such a two-Drude analysis has also been successfully used to describe the optical response of the iron-based superconductors and of other multiband systems (53–55). The broad component typically accounts for a temperature-independent background from nearly incoherent excitations. The temperature dependence of the low-frequency optical response is therefore governed by the narrow Drude component. In analogy, we have first fitted the weight and the scattering rate of the broad D2 component for the spectrum at 100 K and then fixed these parameters for fitting the spectra at lower and higher temperatures. The obtained temperature dependence of the parameters of the D1 component is presented in Fig. 3*C*. Above T^*, the value of $1/\tau_{D1}$ decreases linearly with decreasing temperature, whereas below T^* it follows approximately a $T^{3/2}$ power-law that signals a breakdown of the Fermi liquid behavior. A similar low-temperature power-law behavior occurs in the resistivity data that are displayed in the *Inset* of Fig. 3*A* (solid black line). Also shown, for comparison, are the values of the dc resistivity, $\rho \equiv 1/\sigma_1(\omega \to 0)$, calculated from the fit parameters of the two Drude components (open circles), which agree rather well with those from the transport measurements. The spectral weight of the D1 peak shows a gradual decrease toward low temperature that is anomalously enhanced below $T^* \sim 100$ K. The additional spectra weight loss of the D1 peak can be attributed to the emergence of the M band below T^* which apparently develops at the expense of the D1 peak. This M band has been described by a weak Lorentz band, as shown by the magenta line and shading in Fig. 3*B*. The open squares in Fig. 3*C* confirm that the combined spectral weight of the D1 and M bands does indeed not show a corresponding anomaly in the vicinity of $T^* \sim 100$ K.

The *Inset* of Fig. 3*B* shows the far-infrared response at 10 K with the contribution of the broad Drude peak subtracted. It highlights that the response of the extremely narrow D1 band (with $1/\tau \sim 5$ $cm^{-1} < k_B T \sim 7$ cm^{-1}) and the emerging M band are indeed highly reminiscent of the optical response of a HF system (52, 56). In the latter case, these two components correspond to the intraband response of the heavy quasiparticles and the excitations across the Kondo hybridization gap (Δ), respectively. In analogy, in the following, we assign the M-mode to excitations across a hybridization gap.

The double-peak structure associated with the α and β interband transitions at higher energies has been described with two additional Lorentz terms. Fig. 3*D* details their spectral weight changes with temperature and shows that they have opposite trends and thus nearly cancel each other. This confirms that the high energy spectral weight redistribution occurs predominantly between these α and β bands.

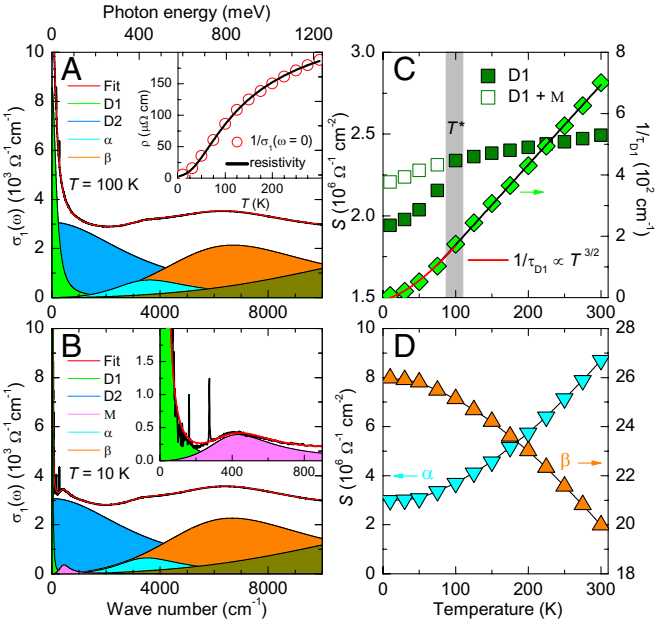

Fig. 3. Decomposition of the optical conductivity spectra of YFe_2Ge_2 at (*A*) $T = 100$ K and (*B*) $T = 10$ K using a Drude–Lorentz model. The *Inset* of panel (*A*) shows a comparison of $1/\sigma_1(\omega \to 0)$, calculated from the Drude-parameters (red circles), and the dc resistivity ρ from transport measurement (black line). The *Inset* of panel (*B*) shows the low-frequency region after subtracting the contribution of the broad Drude peak (D2) to highlight the features of the narrow Drude peak (D1) and the low-energy peak (M). (*C*) Temperature dependence of the fit parameters of the narrow Drude peak (D1). The solid squares show the spectral weight of D1, and the open squares show the combined spectral weight of the D1 and M peaks. The solid diamonds represent the scattering rate of D1. The solid red line shows a fit with a $T^{3/2}$ scaling at low temperatures. (*D*) Temperature-dependent changes of the spectral weight of the α and β bands.

An alternative approach to analyze the low-energy electronic response involves the so-called extended Drude model (EDM). It is typically employed to quantify the renormalization due to electronic correlations in strongly correlated materials. Here, a frequency-dependent mass enhancement $m^*(\omega)/m_b$ and scattering rate $1/\tau(\omega)$ are derived from the measured infrared spectra. Further details about the EDM analysis are provided in *SI Appendix*, section C. The obtained spectra of $1/\tau(\omega)$ and $m^*(\omega)/m_b$ are displayed in Fig. 4 *A* and *B*, respectively. The temperature dependence of the extrapolated zero-frequency values $1/\tau(\omega \to 0)$ and $m^*(\omega \to 0)/m_b$ is shown in Fig. 4 *C* and *D*, respectively. The scattering rate $1/\tau(\omega \to 0)$ exhibits a strong decrease below $T^* \sim 100$ K, which confirms the emergence of a coherent low-temperature state. The corresponding spectra of the effective mass in Fig. 4*B* reveal a sizeable enhancement that becomes very prominent below $T^* \sim 100$ K. The zero-frequency value $m^*(\omega \to 0)/m_b$ in Fig. 4*D* exhibits a clear anomaly below $T^* \sim 100$ K, where it increases more rapidly than above T^* reaching up to $m^*/m_b \sim 10$. This increase signals a sizeable renormalization of (some of) the electronic bands in YFe_2Ge_2 that is reminiscent of the behavior found in other correlated metals such as the HF compounds (57, 58). Note, that this analysis of the optical response only yields an average of the effective mass of the various bands in the vicinity of the Fermi-level which, in case of a strong orbital differentiation, may underestimate the effective mass of a particular band.

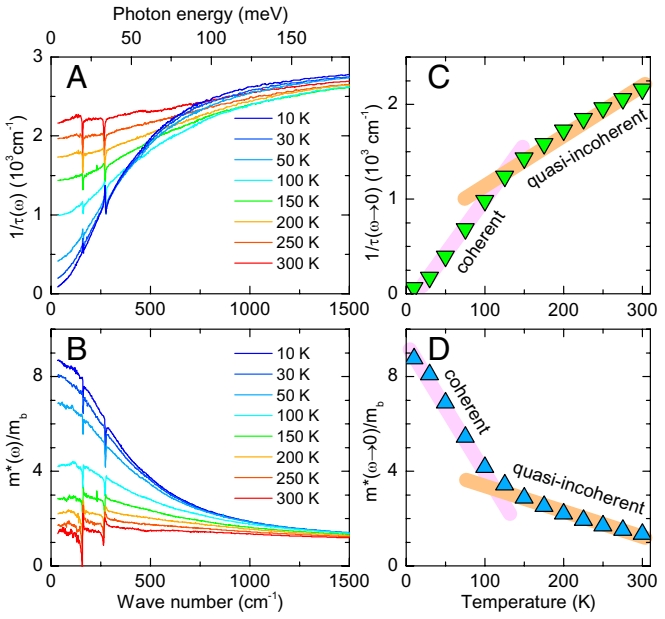

Fig. 4. (*A* and *B*) Spectra of the frequency-dependent scattering rate $1/\tau(\omega)$ and mass enhancement $m^*(\omega)/m_b$, respectively, obtained with an extended Drude model. (*C* and *D*) Temperature dependence of the zero-frequency values $1/\tau(\omega \to 0)$ and $m^*(\omega \to 0)/m_b$, respectively. The colored bars indicate the slope changes around $T^* \sim 100$ K.

To better understand the charge dynamics of YFe_2Ge_2, we have also performed first-principles calculations combining density functional theory (DFT) and dynamical mean-field theory (DMFT). The DFT + DMFT technique has successfully described the electronic structures of many iron-based superconductors (59–61). Fig. 5*A* shows the DFT + DMFT band structure at $T = 40$ K. The first remarkable observation concerns the flat band feature at the Fermi level that extends over a fairly wide momentum range. This flat band is dominated by the $d_{xz/yz}$ orbital character around the M point in the two-iron Brillouin zone representation. As detailed in *SI Appendix*, this flat band region constitutes about 15.6% of the first Brillouin zone. It is noteworthy that recent ARPES measurements have also identified such a flat band feature within a few meV of the Fermi level (49, 50). Another important observation concerns the small hybridization gap between the $d_{xz/yz}$ band and the d_{xy} band that is also in close proximity to the Fermi level. As highlighted in Fig. 5*C*, the size of this hybridization gap amounts to $\Delta \sim 50$ meV. Fig. 5 *C* and *D* compare the band structure and the DOS of the Fe $3d$ orbitals along the Γ–M/M′ directions at $T = 40$ K and 290 K, respectively. Additional calculations for different temperatures can be found in *SI Appendix*, section D. At $T = 40$ K, owing to the flat $d_{xz/yz}$ band, the quasi-particle peak at the Fermi level is sharply defined and resembles that of a so-called Kondo resonance peak. Upon increasing temperature, the quasi-particle peak moves slightly down in energy and undergoes a strong broadening that signals a coherence-incoherence crossover. Note, however, that even at $T = 290$ K the hybridization gap has not entirely vanished, as evidenced by the slight suppression of the DOS in the gap region, and is only smeared out by the band broadening induced by the strong thermal excitations and related effects.

The presence of the flat band and the hybridization gap at the Fermi level naturally explain the main features of the measured infrared conductivity spectra. The calculated $\sigma_1(\omega)$ spectra, as shown in Fig. 2*A*, reproduce quite well the various low-energy intra- and interband excitations. Here, the narrow Drude peak (D1) arises from the intraband excitations of the flat band, while the M band originates from the excitations across the hybridization gap. The substantial temperature dependence of the spectral weight of the α and β bands can also be readily understood, since the α band involves transitions with ∼0.5 eV from the flat band to a higher energy band (cyan arrow), while the β peak is contributed by the transitions with ∼0.75 eV from a lower energy band to the flat band (orange arrow). As the temperature increases, the flat band is broadened and shifted to slightly lower energy which also explains the anomalous blue-shift of the α band. The consequent increase (decrease) of the joint density of states for the α (β) excitations naturally accounts for the observed transfer of spectral weight between these two bands. The development of a coherent state in the flat band is at the heart of the suppression of the scattering rate and the enhancement of the effective mass of the charge carriers seen in Fig. 4 *C* and *D*. Note that the EDM analysis involves contributions from all conduction bands, and therefore yields an averaged value of the quasiparticle effective mass that can be quite a bit smaller than that of the flat band. The infrared data thus agree with recent ARPES and quantum oscillation experiments (48, 49), which yield larger estimates of the quasiparticle effective mass of the flat band of $m^* \sim 25$ to 30 m_0 (m_0 is the bare electron mass).

The flat band and the hybridization gap at the Fermi level in YFe_2Ge_2 thus account for the characteristic features in the optical response that are amazingly similar to those found in Kondo-type HF systems. However, there are also indications that some aspects of the optical response of YFe_2Ge_2 cannot be explained in terms of a classical Kondo scenario. For example, the quasiparticle (Drude) peak and the hybridization gap do not vanish entirely as the temperature is increased above T^*, but are only blurred due to the broadening of these bands. In return, this implies that a classical Kondo hybridization scenario does not entirely explain the behavior of the flat band and the hybridization gap in YFe_2Ge_2. Moreover, it indicates that the Fe $3d_{xz/yz}$ electrons are not fully localized at high temperatures and, accordingly, this compound does not appear to be in the Kondo limit.

Notably, even for the comparison of YFe_2Ge_2 and KFe_2As_2 it appears that, despite their strikingly similar infrared response (details are shown in *SI Appendix*, section H), different mechanisms are causing the flat band formation and the related HF behavior. For KFe_2As_2, it was previously reported that the HF behavior originates from a large Hund's coupling which leads to a strong orbital differentiation of the electron correlations (31, 33–35). Such a Hund's metal scenario is indeed feasible in case of KFe_2As_2 with an orbital occupancy of $3d^{5.5}$ that is rather close to a half-filling (at $3d^5$). In KFe_2As_2, the mass enhancement of the d_{xy} orbital has been reported to reach values as high as 15 to 20 and to exceed that of the $d_{xz/yz}$ levels by at least a factor of three (31). The strong differentiation of orbital-selective correlations thus can explain the coexistence of light and heavy d electrons, and thus the analogy to the classical f-electron HF systems, where this role is played by the s and f electrons.

A different scenario arises for YFe_2Ge_2, where the orbital-resolved mass enhancement and orbital-selective correlations, as obtained from our DFT + DMFT calculations and shown in Fig. 6, appear to be weaker than in KFe_2As_2. For the d_{z^2} and $d_{x^2-y^2}$ orbitals, which are anyhow far away from the Fermi level, the mass enhancement is only moderate with $m^*/m_b \sim 2$ to 3 and hardly temperature dependent. The most relevant

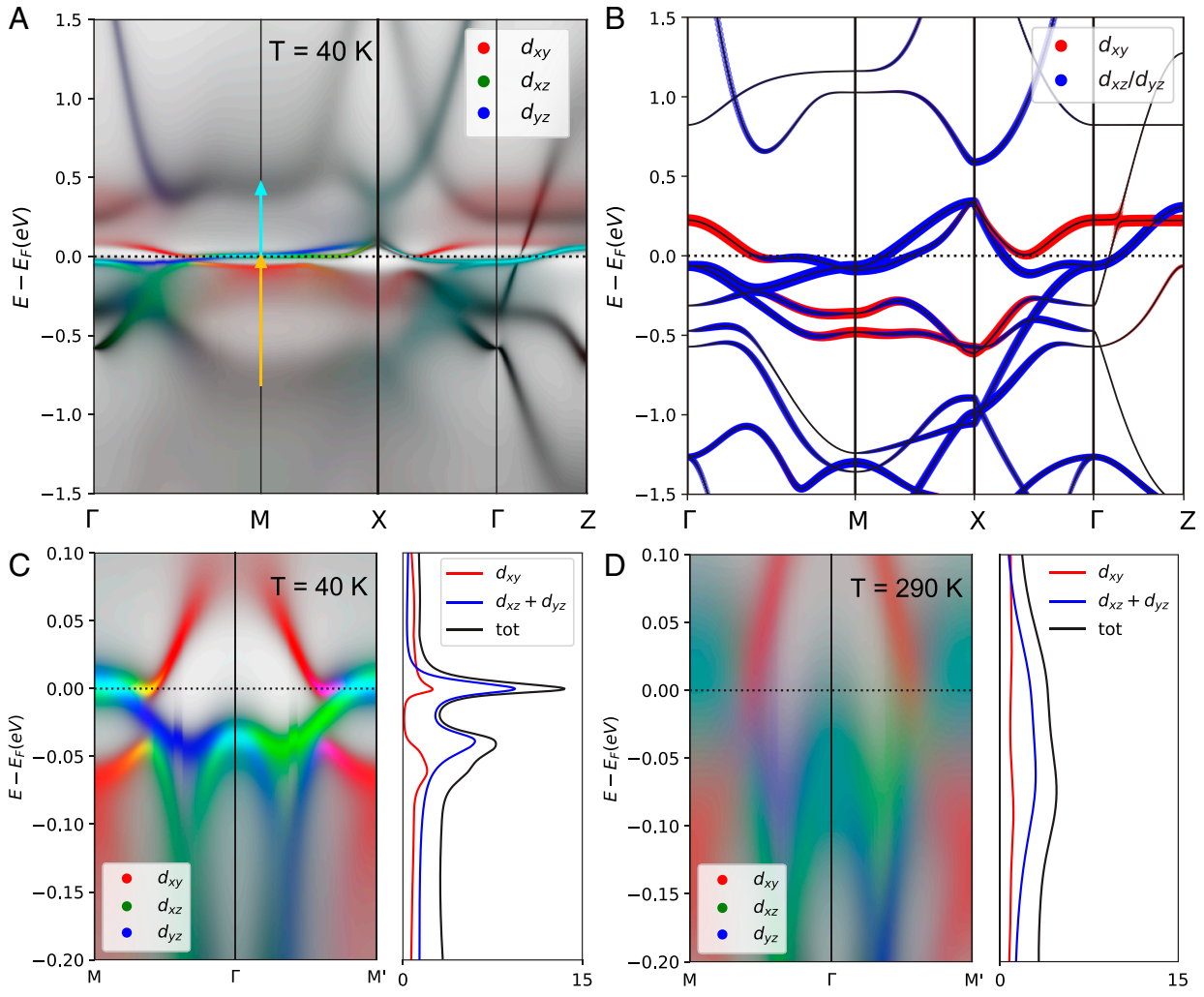

Fig. 5. (*A*) Orbital-resolved electronic band structure of YFe_2Ge_2 obtained by the DFT + DMFT method at $T = 40$ K. Arrows indicate the corresponding optical transitions for the α and β bands in the infrared spectra. (*B*) Orbital-resolved electronic band structure calculated with the DFT method, which underestimates electronic correlations. (*C* and *D*) Orbital-resolved electronic structure and DOS along the Γ–M/M′ directions near the Fermi level obtained by the DFT + DMFT method at $T = 40$ K and 290 K, respectively.

d_{xy} and $d_{xz/yz}$ orbitals have rather similar mass enhancement factors that amount to about ∼3.5 at $T = 386$ K and exhibit a moderate increase to ∼5 to 6 at low temperature. This confirms that in YFe_2Ge_2 there is only quite a weak differentiation of the mass enhancement of the relevant bands in the vicinity of the Fermi-level, which can hardly explain the flat band and HF behavior.

To gain more insight into the origin of the flat band and the related HF state in YFe_2Ge_2, we conducted a more careful comparison between YFe_2Ge_2 and KFe_2As_2. As detailed in *SI Appendix*, section H, a comparison of the DFT band structures of YFe_2Ge_2 and KFe_2As_2 reveals that the *d* bands in the vicinity of the Fermi level are much narrower for the former than for the latter. The reason for the band flattening in the absence of electronic correlations in YFe_2Ge_2 is a so-called kinetic frustration effect (59). This arises due to a competition between the direct Fe-Fe and the indirect Fe-Ge-Fe hopping channels for which the hopping parameters have opposite signs and thus give rise to a strongly destructive interference effect when they have comparable amplitudes, as is the case in YFe_2Ge_2 for which the collapsed 122-structure yields a stronger Fe-Ge bonding and thus an enhanced Fe-Ge-Fe hopping parameter (as compared to the uncollapsed 122-structure of KFe_2As_2). Note that, in addition to the orbital occupancy (31), the anisotropy of the direct and indirect hopping parameters is also an important factor contributing to the orbital differentiation (59). Therefore,

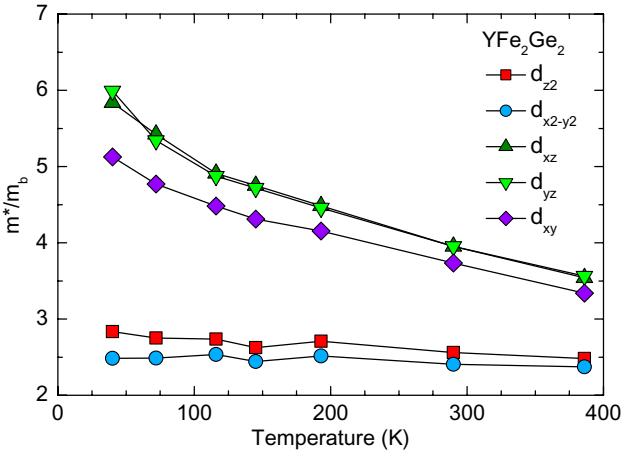

Fig. 6. Temperature dependence of the orbital-resolved mass enhancement for YFe_2Ge_2 obtained from the DFT + DMFT calculations.

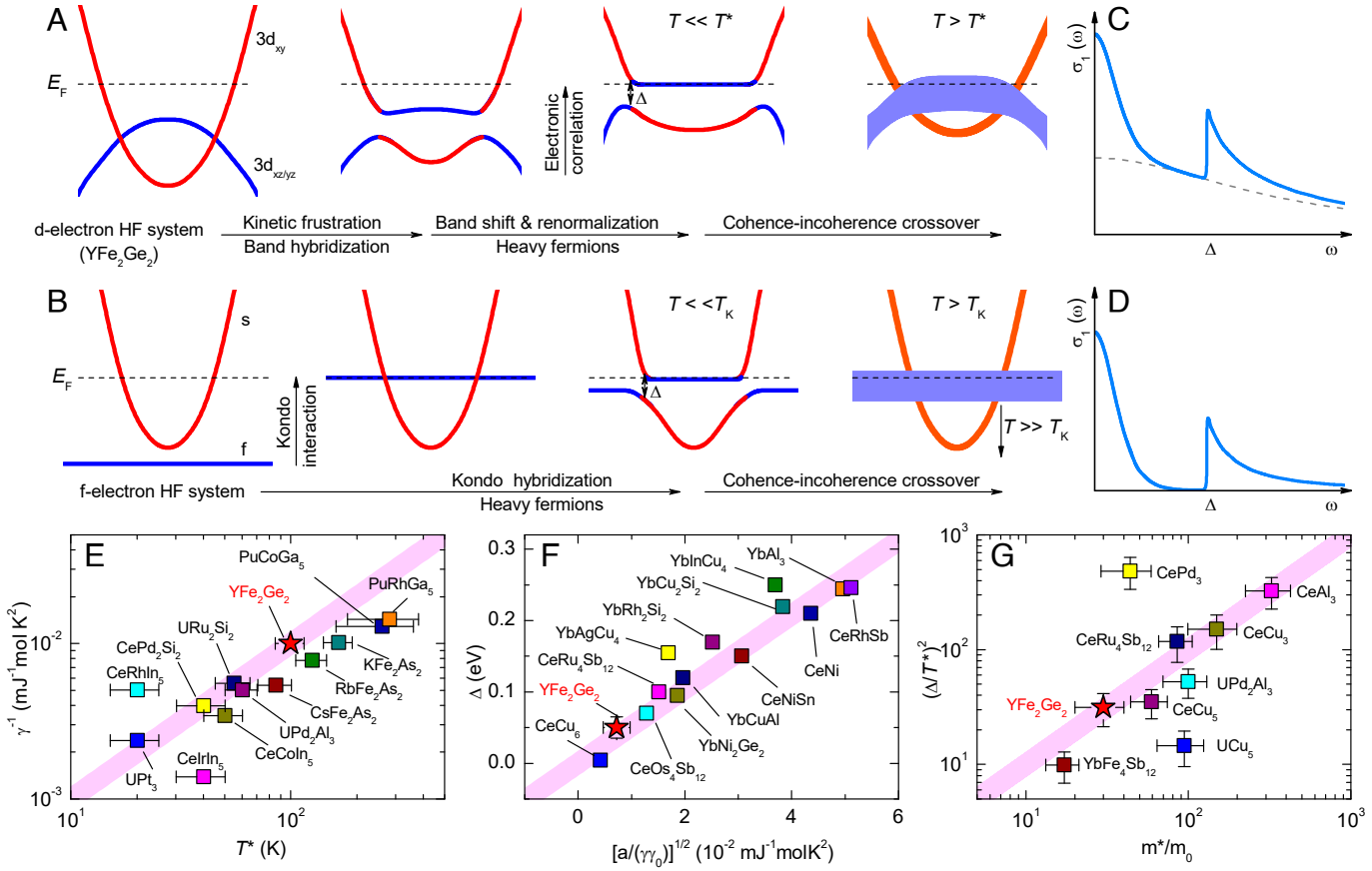

Fig. 7. (*A* and *B*) Schematics of the development of a flat band and hybridization gap at the Fermi level in *d*-electron and *f*-electron systems, respectively. (*C* and *D*) Corresponding $\sigma_1(\omega)$ spectra in the HF state for the coherent Drude response of heavy quasiparticles and excitations across the hybridization gap. The dashed gray line in (*C*) denotes a broad Drude response from other incoherent *d*-electron bands. (*E*–*G*) Scaling plots of γ^{-1} vs. T^*, Δ vs. $[a/(\gamma\gamma_0)]^{1/2}$, and $(\Delta/T^*)^2$ vs. m^*/m_0, respectively, for various HF compounds. The red star shows the corresponding scaling behavior of YFe_2Ge_2. The values for the other HF compounds have been adopted from refs. 27, 57, and 63 and references cited therein.

the weak anisotropy in hopping parameters for YFe_2Ge_2 also accounts for the weak orbital differentiation within the $d_{xz/yz}$ and d_{xy}, as observed in Fig. 6.

A second crucial factor is band hybridization, as is evident from both the DFT + DMFT and the DFT band structures, shown in Fig. 5 *A* and *B*, respectively, which reveals that the hybridization of the $d_{xz/yz}$ and d_{xy} bands (and the resulting small hybridization gap) appears in both cases. As outlined in *SI Appendix*, section H, this hybridization is facilitated by the partial occupation and the extended spatial expansion of the Y 4*d* electrons, enabling them to overlap with Fe 3*d* electrons. Consequently, the *d* orbitals near the Fermi level hybridize, further flattening the bands. In comparing the DFT + DMFT and the DFT results, the influence of the electron correlations, particularly of the orbital-selective ones, appears to be a secondary effect that helps to further flatten these bands and shift them closer toward the Fermi level, where they become electronically active (62).

Fig. 7*A* shows a schematic summary of the above-described scenario for obtaining a flat band and hybridization gap at the Fermi level of YFe_2Ge_2. Fig. 7*B* displays a corresponding sketch of the classical Kondo effect. Despite their different mechanisms, the two cases yield a very similar electronic structure of the HF state, i.e., featuring a flat band and a hybridization gap at the Fermi level. Accordingly, as illustrated in Fig. 7 *C* and *D*, the *d*-electron and *f*-electron HF states both share very similar spectral features in the optical conductivity. Notably, for the *d*-electron HF state these features are superimposed on an additional broad Drude peak due to contributions from other *d*-electron bands that remain incoherent.

Next, we address the question whether, despite of the above discussed different mechanism of the flat band and HF behavior in YFe_2Ge_2, the scaling relationships of the *f*-electron HF compounds are still obeyed. In the following, we show that this is indeed the case. In the *f*-electron HF compounds the following scaling relation between the Sommerfeld coefficient γ and the Kondo temperature T_K (or the crossover temperature T^*) applies: $T_K = \mathrm{R}\log 2/\gamma \simeq 10^4/\gamma$ [$\mathrm{mJ^{-1}\ mol\ K^2}$] (26, 27, 64). Fig. 7*E* shows that this $T^* \sim 1/\gamma$ scaling is also observed in YFe_2Ge_2 with $T^* \simeq 100$ K and a value of $\gamma \simeq 100$ $\mathrm{mJ\ mol^{-1}K^{-2}}$, as reported from specific heat (43). Additional scaling relations, that have been derived from the hybridization of the conduction and the *f* electrons by using the mean-field approximation to the periodic Anderson model (52, 57, 63, 65), are $\Delta \propto \sqrt{T_K W}$ and $m^*/m_0 = (\Delta/T_K)^2$. Here, Δ is the direct hybridization gap, W the conduction electron bandwidth, and m^*/m_0 the effective mass of the heavy electrons. The scaling relation $\Delta \propto \sqrt{T_K W}$ can be rewritten as $\Delta \propto \sqrt{a/(\gamma\gamma_0)}$. This has been demonstrated by Okamura *et al* for a number of Ce- and Yb-based HF compounds, where W of a Ce(Yb) HF compound can be regarded as inversely proportional to γ of the isostructural La(Lu) non-HF compound (denoted as γ_0), and a is a constant

which depends only on the f level degeneracy N: $a = 0.21, 0.54$, and 0.59 for $N = 2$, 6, and 8, respectively (52, 63). Fig. 7 F and G show that YFe_2Ge_2 does indeed obey the scaling relations of $\Delta \propto \sqrt{a/(\gamma\gamma_0)}$ and $m^*/m_0 = (\Delta/T^*)^2$, with the parameters $\Delta \simeq 50$ meV, $\gamma \simeq 100$ mJ mol^{-1}K^{-2}, $\gamma_0 \simeq 40$ mJ mol^{-1}K^{-2} [from specific heat data of LaFe2Ge2 (43, 66)], $a = 0.21$ for a doublet degeneracy, $m^*/m_0 \simeq 30$ (48, 49), and $T^* \simeq 100$ K.

Finally, we comment on the significance of our findings. The proposed mechanism and its similarity to the Kondo scenario not only sheds light on the origin of HF state in YFe_2Ge_2, but also offers insights to clarify its Kondo-like properties. The emergent flat band at the Fermi level may also account for various exotic properties of YFe_2Ge_2, such as the non-Fermi-liquid behavior (67), the coexistence of FM and AFM spin fluctuations (47, 62), the large Sommerfeld coefficient at low temperatures (49, 50) (which is also reproduced by our calculations provided in *SI Appendix*, section F), and even the occurrence of unconventional superconductivity (68). On the other hand, our scenario suggests a novel route to construct and manipulate flat bands through the combined interactions of kinetic frustrations, band hybridization, and electron correlations, which can improve the participation of flat bands in the low-energy physics. Furthermore, taking into account the topology of band hybridization, this scenario will be interesting for building a rich set of novel topological quantum phenomena, such as possible topological HF state or topological superconductivity (69). In conclusion, the present work identifies YFe_2Ge_2 as a model system that can serve as a platform for investigating the d-electron HF physics and related exotic properties.

Materials and Methods

High-quality single crystals of YFe_2Ge_2 were grown with a Sn-flux method, and details of sample characterization were provided in ref. 47. The resistivity vs. temperature was measured with a commercial Physical Properties Measurement System (Quantum Design PPMS), as shown in the *Inset* of Fig. 3*A*. Temperature-dependent infrared reflectance measurements were performed on flat shiny facets using a Bruker VERTEX 70v Fourier transform infrared spectrometer with an in situ gold overfilling technique (70) (*SI Appendix*, section A has the experimental details). The combination of density functional theory and dynamical mean field theory (DFT + DMFT) (71, 72) is employed to calculate the many-body electronic structure (*SI Appendix*, section D has the computational details).

Data, Materials, and Software Availability. All study data are included in the article and/or *SI Appendix*.

ACKNOWLEDGMENTS. This work was supported by the National Natural Science Foundation of China (Grant No. 12274442) and the National Key Research and Development Program of China (Grant No. 2022YFA1403901), as well as by the Swiss National Science Foundation through Grants No. 200020-172611 and 200021-214905. Z.Y. and R.L. were supported by the Fundamental Research Funds for the Central Universities (Grant No. 2243300003), the Innovation Program for Quantum Science and Technology (Grant No. 2021ZD0302800), and the National Natural Science Foundation of China (Grant No. 12074041). The DFT+DMFT calculations were carried out with high-performance computing cluster of Beijing Normal University in Zhuhai. J.Z. was supported by the Key Program of National Natural Science Foundation of China (Grant No. 12234006), National Key Research and Development Program of China (Grant No. 2022YFA14032), and the Innovation Program for Quantum Science and Technology (Grant No. 2024ZD0300103). H.W. was supported by the Youth Foundation of the National Natural Science Foundation of China (Grant No. 12204108).

Author affiliations: [a]Beijing National Laboratory for Condensed Matter Physics, Institute of Physics, Chinese Academy of Sciences, Beijing 100190, China; [b]School of Physical Sciences, University of Chinese Academy of Sciences, Beijing 100049, China; [c]Department of Physics and Fribourg Center for Nanomaterials, University of Fribourg, Fribourg CH-1700, Switzerland; [d]School of Physics and Astronomy and Center for Advanced Quantum Studies, Beijing Normal University, Beijing 100875, China; [e]State Key Laboratory of Surface Physics and Department of Physics, Fudan University, Shanghai 200433, China; and [f]Key Laboratory of Multiscale Spin Physics (Ministry of Education), Beijing Normal University, Beijing 100875, China

1. E. H. Lieb, Two theorems on the hubbard model. *Phys. Rev. Lett.* **62**, 1927–1927 (1989).
2. A. L. Sharpe *et al.*, Emergent ferromagnetism near three-quarters filling in twisted bilayer graphene. *Science* **365**, 605–608 (2019).
3. G. R. Stewart, Non-Fermi-liquid behavior in *d*- and *f*-electron metals. *Rev. Mod. Phys.* **73**, 797–855 (2001).
4. J. S. Hofmann, E. Berg, D. Chowdhury, Superconductivity, charge density wave, and supersolidity in flat bands with a tunable quantum metric. *Phys. Rev. Lett.* **130**, 226001 (2023).
5. N. Regnault, B. A. Bernevig, Fractional chern insulator. *Phys. Rev. X* **1**, 021014 (2011).
6. T. Neupert, L. Santos, C. Chamon, C. Mudry, Fractional quantum Hall states at zero magnetic field. *Phys. Rev. Lett.* **106**, 236804 (2011).
7. Y. Xie *et al.*, Fractional Chern insulators in magic-angle twisted bilayer graphene. *Nature* **600**, 439–443 (2021).
8. Y. Cao *et al.*, Correlated insulator behaviour at half-filling in magic-angle graphene superlattices. *Nature* **556**, 80–84 (2018).
9. Y. Cao *et al.*, Unconventional superconductivity in magic-angle graphene superlattices. *Nature* **556**, 43–50 (2018).
10. J. X. Yin, B. Lian, M. Z. Hasan, Topological kagome magnets and superconductors. *Nature* **612**, 647–657 (2022).
11. E. Liu *et al.*, Giant anomalous Hall effect in a ferromagnetic kagome-lattice semimetal. *Nat. Phys.* **14**, 1125–1131 (2018).
12. J. X. X. Yin *et al.*, Negative flat band magnetism in a spin-orbit-coupled correlated kagome magnet. *Nat. Phys.* **15**, 443–448 (2019).
13. B. R. Ortiz *et al.*, CsV_3Sb_5: A Z_2 topological kagome metal with a superconducting ground state. *Phys. Rev. Lett.* **125**, 247002 (2020).
14. H. Chen *et al.*, Roton pair density wave in a strong-coupling kagome superconductor. *Nature* **599**, 222–228 (2021).
15. L. Nie *et al.*, Charge-density-wave-driven electronic nematicity in a kagome superconductor. *Nature* **604**, 59–64 (2022).
16. J. X. Yin *et al.*, Quantum-limit Chern topological magnetism in $TbMn_6Sn_6$. *Nature* **583**, 533–536 (2020).
17. M. Kang *et al.*, Topological flat bands in frustrated kagome lattice CoSn. *Nat. Commun.* **11**, 4004 (2020).
18. Z. Liu *et al.*, Orbital-selective Dirac fermions and extremely flat bands in frustrated kagome-lattice metal CoSn. *Nat. Commun.* **11**, 4002 (2020).
19. X. Teng *et al.*, Discovery of charge density wave in a kagome lattice antiferromagnet. *Nature* **609**, 490–495 (2022).
20. G. R. Stewart, Heavy-fermion systems. *Rev. Mod. Phys.* **56**, 755–787 (1984).
21. J. G. Cheng *et al.*, Possible kondo physics near a metal-insulator crossover in the *A*-Site ordered perovskite $CaCu_3Ir_4O_{12}$. *Phys. Rev. Lett.* **111**, 176403 (2013).
22. W. Kobayashi, I. Terasaki, J. Takeya, I. Tsukada, Y. Ando, A novel heavy-fermion State in $CaCu_3Ru_4O_12$. *J. Phys. Soc. Jpn.* **73**, 2373–2376 (2004).
23. H. Liu *et al.*, Observation of flat bands due to band hybridization in the 3*d*-electron heavy-fermion compound $CaCu_3Ru_4O_{12}$. *Phys. Rev. B* **102**, 035111 (2020).
24. M. Kim *et al.*, Signature of Kondo hybridisation with an orbital-selective Mott phase in 4d $Ca_{2-x}Sr_xRuO_4$. *NPJ Quantum Mater.* **7**, 59 (2022).
25. S. Kondo *et al.*, LiV_2O_4: A heavy fermion transition metal oxide. *Phys. Rev. Lett.* **78**, 3729–3732 (1997).
26. Y. Zhang *et al.*, Emergence of Kondo lattice behavior in a van der Waals itinerant ferromagnet Fe_3GeTe_2. *Sci. Adv.* **4**, eaao6791 (2018).
27. Y. P. Wu *et al.*, Emergent Kondo lattice behavior in iron-based superconductors AFe_2As_2 (A = K, Rb, Cs). *Phys. Rev. Lett.* **116**, 147001 (2016).
28. Y. Kim *et al.*, Kondo interaction in FeTe and its potential role in the magnetic order. *Nat. Commun.* **14**, 4145 (2023).
29. L. de' Medici, Hund's coupling and its key role in tuning multiorbital correlations. *Phys. Rev. B* **83**, 205112 (2011).
30. A. Georges, L. Medici, J. Mravlje, Strong correlations from hund's coupling. *Annu. Rev. Condens. Matter Phys.* **4**, 137–178 (2013).
31. L. de' Medici, G. Giovannetti, M. Capone, Selective Mott physics as a key to iron superconductors. *Phys. Rev. Lett.* **112**, 177001 (2014).
32. J. S. Kim, E. G. Kim, G. R. Stewart, X. H. Chen, X. F. Wang, Specific heat in KFe_2As_2 in zero and applied magnetic field. *Phys. Rev. B* **83**, 172502 (2011).
33. T. Terashima *et al.*, Fermi surface and mass enhancement in KFe_2As_2 from de Haas-van Alphen effect measurements. *J. Phys. Soc. Jpn.* **79**, 053702 (2010).
34. T. Terashima *et al.*, Fermi surface in KFe_2As_2 determined via de Haas-van Alphen oscillation measurements. *Phys. Rev. B* **87**, 224512 (2013).
35. T. Sato *et al.*, Band structure and fermi surface of an extremely overdoped iron-based superconductor KFe_2As_2. *Phys. Rev. Lett.* **103**, 047002 (2009).

36. F. Hardy *et al*., Evidence of strong correlations and coherence-incoherence crossover in the iron pnictide superconductor KFe_2As_2. *Phys. Rev. Lett.* **111**, 027002 (2013).
37. P. Wiecki *et al*., Pressure dependence of coherence-incoherence crossover behavior in KFe_2As_2 observed by resistivity and ^{75}As-NMR/NQR. *Phys. Rev. B* **97**, 064509 (2018).
38. D. J. Singh, Superconductivity and magnetism in YFe_2Ge_2. *Phys. Rev. B* **89**, 024505 (2014).
39. J. Chen *et al*., Unconventional superconductivity in the layered iron germanide YFe_2Ge_2. *Phys. Rev. Lett.* **116**, 127001 (2016).
40. Y. Zou *et al*., Fermi liquid breakdown and evidence for superconductivity in YFe_2Ge_2. *Phys. Stat. Solid.* **8**, 928–930 (2014).
41. A. Subedi, Unconventional sign-changing superconductivity near quantum criticality in YFe_2Ge_2. *Phys. Rev. B* **89**, 024504 (2014).
42. J. Chen, M. B. Gamża, K. Semeniuk, F. M. Grosche, Composition dependence of bulk superconductivity in YFe_2Ge_2. *Phys. Rev. B* **99**, 020501 (2019).
43. J. Chen *et al*., Unconventional bulk superconductivity in YFe_2Ge_2 single crystals. *Phys. Rev. Lett.* **125**, 237002 (2020).
44. D. Zhao *et al*., Approaching itinerant magnetic quantum criticality through a Hund's coupling induced electronic crossover in the YFe_2Ge_2 superconductor. *Phys. Rev. B* **101**, 064511 (2020).
45. N. Sirica *et al*., Spectroscopic evidence for strong quantum spin fluctuations with itinerant character in YFe_2Ge_2. *Phys. Rev. B* **91**, 121102 (2015).
46. J. Ferstl, H. Rosner, C. Geibel, Evidence for fluctuating Fe-moments in RFe_2Ge_2 (R = Lu, Yb). *Phys. B Condens. Matter* **378–380**, 744–745 (2006).
47. H. Wo *et al*., Coexistence of ferromagnetic and stripe-type antiferromagnetic spin fluctuations in YFe_2Ge_2. *Phys. Rev. Lett.* **122**, 217003 (2019).
48. J. Baglo *et al*., Fermi surface and mass renormalization in the iron-based superconductor YFe_2Ge_2. *Phys. Rev. Lett.* **129**, 046402 (2022).
49. R. Kurleto *et al*., Flat bands at the fermi level in unconventional superconductor YFe_2Ge_2. arXiv [Preprint] (2023). http://arxiv.org/abs/2311.09492 (Accessed 16 November 2023).
50. D. F. Xu *et al*., Electronic structure of YFe_2Ge_2 studied by angle-resolved photoemission spectroscopy. *Phys. Rev. B* **93**, 024506 (2016).
51. G. Bossé *et al*., Anomalous frequency and temperature-dependent scattering and Hund's coupling in the almost quantum critical heavy-fermion system $CeFe_2Ge_2$. *Phys. Rev. B* **93**, 085104 (2016).
52. R. Y. Chen, N. L. Wang, Infrared properties of heavy fermions: Evolution from weak to strong hybridizations. *Rep. Prog. Phys.* **79**, 064502 (2016).
53. D. Wu *et al*., Optical investigations of the normal and superconducting states reveal two electronic subsystems in iron pnictides. *Phys. Rev. B* **81**, 100512 (2010).
54. Y. M. Dai *et al*., Hidden *T*-linear scattering rate in $Ba_{0.6}\mathbf{K}_{0.4}Fe_2As_2$ revealed by optical spectroscopy. *Phys. Rev. Lett.* **111**, 117001 (2013).
55. B. Xu *et al*., Infrared probe of the gap evolution across the phase diagram of $Ba_{1-x}K_xFe_2As_2$. *Phys. Rev. B* **96**, 115125 (2017).
56. E. J. Singley, D. N. Basov, E. D. Bauer, M. B. Maple, Optical conductivity of the heavy fermion superconductor $CeCoIn_5$. *Phys. Rev. B* **65**, 161101 (2002).
57. S. V. Dordevic, D. N. Basov, N. R. Dilley, E. D. Bauer, M. B. Maple, Hybridization gap in heavy fermion compounds. *Phys. Rev. Lett.* **86**, 684–687 (2001).
58. D. N. Basov, R. D. Averitt, D. van der Marel, M. Dressel, K. Haule, Electrodynamics of correlated electron materials. *Rev. Mod. Phys.* **83**, 471–541 (2011).
59. Z. P. Yin, K. Haule, G. Kotliar, Kinetic frustration and the nature of the magnetic and paramagnetic states in iron pnictides and iron chalcogenides. *Nat. Mater.* **10**, 932–935 (2011).
60. Z. P. Yin, K. Haule, G. Kotliar, Magnetism and charge dynamics in iron pnictides. *Nat. Phys.* **7**, 294–297 (2011).
61. Z. P. Yin, K. Haule, G. Kotliar, Spin dynamics and orbital-antiphase pairing symmetry in iron-based superconductors. *Nat. Phys.* **10**, 845–850 (2014).
62. H. Mao *et al*., Topological states and competing magnetic fluctuations in iron germanides. *Phys. Rev. B* **107**, 115116 (2023).
63. H. Okamura *et al*., Universal scaling in the dynamical conductivity of heavy fermion Ce and Yb compounds. *J. Phys. Soc. Jpn.* **76**, 1–5 (2007).
64. Y. Ōnuki *et al*., Heavy fermions and unconventional superconductivity in high-quality single crystals of rare-earth and actinide compounds. *J. Korean Phys. Soc.* **63**, 409–415 (2013).
65. A. J. Millis, P. A. Lee, Large-orbital-degeneracy expansion for the lattice anderson model. *Phys. Rev. B* **35**, 3394–3414 (1987).
66. T. Ebihara *et al*., Magnetic properties of single crystal $CeFe_2Ge_2$. *Phys. B* **206–207**, 219–221 (1995).
67. P. Kumar, S. Peotta, Y. Takasu, Y. Takahashi, P. Törmä, Flat-band-induced non-Fermi-liquid behavior of multicomponent fermions. *Phys. Rev. A* **103**, L031301 (2021).
68. Y. Cao, Y. Yang, Flat bands promoted by Hund's rule coupling in the candidate double-layer high-temperature superconductor $La_3Ni_2O_7$ under high pressure. *Phys. Rev. B* **109**, L081105 (2024).
69. N. Hao, J. Hu, Topological quantum states of matter in iron-based superconductors: From concept to material realization. *Natl. Sci. Rev.* **6**, 213–226 (2019).
70. C. C. Homes, M. Reedyk, D. A. Cradles, T. Timusk, Technique for measuring the reflectance of irregular, submillimeter-sized samples. *Appl. Opt.* **32**, 2976–2983 (1993).
71. G. Kotliar *et al*., Electronic structure calculations with dynamical mean-field theory. *Rev. Mod. Phys.* **78**, 865–951 (2006).
72. K. Haule, C. H. Yee, K. Kim, Dynamical mean-field theory within the full-potential methods: Electronic structure of $CeIrIn_5$, $CeCoIn_5$, and $CeRhIn_5$. *Phys. Rev. B* **81**, 195107 (2010).